Electronic Supplementary Material (ESI) for Lab on a Chip.

# Supporting Information

# Continuous-flow label-free size fractionation of extracellular vesicles through electrothermal fluid rolls and dielectrophoresis synergistically integrated in a microfluidic device

*Yang Bu,*[1] *Jinhui Wang,*[2] *Sheng Ni,*[1] *Yusong Guo,*[2] *and Levent Yobas* [1,3,*]

[1]Department of Electronic and Computer Engineering,

[2]Division of Life Sciences,

[3]Department of Chemical and Biological Engineering,

The Hong Kong University of Science and Technology,

Clear Water Bay, Hong Kong SAR, China.

[*]E-mail: eelyobas@ust.hk

Contents:

# THEORY

Electrothermal flow (ETF) occurs in a liquid when a non-uniform electric field causes uneven Joule heating, resulting in thermal gradients that create permittivity and conductivity gradients.[1] These gradients then give rise to an electrical bulk force, which drives fluid motion. The electric field $\boldsymbol{E}$ can be calculated by co-solving Gauss' law:

$$\nabla \cdot (\varepsilon \boldsymbol{E}) = \rho_{\mathrm{c}} \tag{S–1}$$

charge density continuity equation,

$$\frac{\partial \rho_{\mathrm{c}}}{\partial t} + \nabla \cdot \boldsymbol{J} = 0 \tag{S–2}$$

Ohm's law,

$$\boldsymbol{J} = \sigma \boldsymbol{E} \tag{S–3}$$

and Faraday's law,

$$\nabla \times \boldsymbol{E} = 0 \tag{S–4}$$

where $\varepsilon$ is the medium electrical permittivity, $\sigma$ the medium electrical conductivity and $\rho_{\mathrm{c}}$ the local charge density, $\boldsymbol{J}$ the current density, and $\nabla$ the vector differential (del) operator.

Joule heating is induced in the medium in response to an electric field and the heat generation per unit volume can be expressed as:

$$P = \sigma \boldsymbol{E}^2 \tag{S–5}$$

and the temperature $T$ distribution can be obtained from:[2]

$$\rho_m C \left( \frac{\partial T}{\partial t} + \boldsymbol{u} \cdot \nabla T \right) = k \nabla^2 T + P \tag{S–6}$$

where $\rho_m$, $C$, and $k$ denote mass density, specific heat, and thermal conductivity of the medium, and $\boldsymbol{u}$ the velocity vector field. The electric field and temperature field obtained from above equations can hence be used to obtain the time-averaged electrothermal force:

$$\langle \boldsymbol{F}_{\mathrm{ETF}} \rangle = \frac{1}{2} \cdot \frac{\varepsilon(\alpha-\beta)}{1+\left(\frac{\omega\varepsilon}{\sigma}\right)^2} (\nabla T \cdot \boldsymbol{E})\boldsymbol{E} - \frac{1}{4}\varepsilon\alpha|\boldsymbol{E}|^2 \tag{S–7}$$

where $\omega = 2\pi f$ is the angular frequency of the electrical field with $f$ being the ordinary frequency and $\alpha = (\partial\varepsilon/\partial T)/\varepsilon$ and $\beta = (\partial\sigma/\partial T)/\sigma$ represent respective thermal gradient in the electrical permittivity and the electrical conductivity of the medium, respectively.

The velocity field is modeled by the Stokes equation at low Reynolds number,

$$0 = -\nabla p + \eta\nabla^2\boldsymbol{u} + \boldsymbol{F}_{\mathrm{ETF}} \tag{S–8}$$

and the continuity equation,

$$\nabla \cdot \boldsymbol{u} = 0 \tag{S–9}$$

where $p$ is the pressure and $\eta$ the dynamic viscosity of the medium.

Hydrodynamic drag force acting on a rigid particle in a viscous fluid at a relatively low speed is expressed by the Stokes' drag equation:

$$\boldsymbol{F}_{\mathrm{drag}} = 6\pi\eta(\boldsymbol{u} - \boldsymbol{u}_p)R \tag{S–10}$$

where $\boldsymbol{u}_p$ is the velocity vector of particle and $R$ the particle radius.

Time-averaged DEP force exerted on a spherical particle in a medium in the presence of a non-uniform electric field $\boldsymbol{E}$ can be written as:[3]

$$\langle \boldsymbol{F}_{\mathrm{DEP}} \rangle = 2\pi\varepsilon R^3 \mathrm{Re}[f_{CM}(\omega)]\nabla(|\boldsymbol{E}|^2) \tag{S–11}$$

where $\mathrm{Re}[f_{CM}(\omega)]$ is the real part of the Clausius-Mossotti (CM) factor, which represents the frequency-dependent complex polarizability of the particle in relation to that of the medium:[4]

$$f_{CM}(\omega) = \frac{\varepsilon_p^* - \varepsilon^*}{\varepsilon_p^* + 2\varepsilon^*} \tag{S–12}$$

where $\varepsilon_p^*$ and $\varepsilon^*$ are the particle and medium complex permittivities with real parts defined by absolute permittivities $\varepsilon_p$ and $\varepsilon$ and imaginary parts by $-\sigma_p/\omega$, and $-\sigma/\omega$ with $\sigma_p$ and $\sigma$ referring to respective conductivities. The polarity and direction of the DEP force is determined by the sign of $\mathrm{Re}[f_{CM}(\omega)]$: $\mathrm{Re}[f_{CM}(\omega)] > 0$ signifies positive DEP (pDEP) with the particle moving up the field gradient whereas $\mathrm{Re}[f_{CM}(\omega)] < 0$ signifies negative DEP (nDEP) with the particle moving down the field gradient. The switch in polarity occurs at a so-called crossover frequency $\omega_c$, where $\mathrm{Re}[f_{CM}(\omega_c)] = 0$ and the particle ceases to experience any DEP force.[5]

At the electric field frequencies below 10 MHz, the particle polarization is determined by:[6]

$$f_{CM}(\omega) = \frac{\sigma_p - \sigma}{\sigma_p + 2\sigma} \tag{S–13}$$

where the conductivity $\sigma_p$ of a homogeneous solid spherical particle, is a combination of bulk conductivity, $\sigma_b$ and surface conductivity $\sigma_s$. For submicron particles or nanoparticles, $\sigma_s$ may have a significant impact on the dielectrophoretic behavior. In the case of polystyrene (PS) submicron particles, bulk conductivity is negligible compared to surface conductivity, and particle conductivity is predominantly influenced by the charges in the electrical double layer.

We model PS particles and extracellular vesicles (EVs) based on a single-shell dielectric model consisting of an insulating core of radius $R$ of low conductivity and permittivity with a conductive shell of thickness $\kappa^{-1}$ due to the electrical double layer. The particle conductivity can be expressed as:[7]

$$\sigma_p = \sigma_b + 2\frac{K_{stern}}{R} + 2\frac{K_{diff}}{R} \tag{S–14}$$

where $\sigma_b$ is the particle bulk conductivity, $K_{stern}$ and $K_{diff}$ represent the Stern layer conductance and the diffuse layer conductance, respectively.

The Stern layer conductance can be calculated as:[8]

$$K_{Stern} = \frac{\rho_q \mu_s \sigma}{2zFc\mu_m}, \tag{S–15}$$

where $\rho_q$ is the surface charge density, $\mu_s$ and $\mu_m$ the mobility of ion species in the Stern layer and bulk medium, respectively, $z$ the valence of the counterion, $F$ the Faraday constant and $c$ the electrolyte concentration. The surface charge density $\rho_q$ for latex particles falls in the range of 22-40 mC/m$^2$, which results in a conductance value of approximately 1 nS.[7-9] The reported surface charge density $\rho_q$ for EVs is around –6.2 mC/m$^2$,[10-11] which leads to a $K_{Stern}$ value of approximately 0.2 nS, based on eq (S-15).

The diffuse layer conductance can be written as[7]

$$K_{diff} = \frac{4F^2cz^2D(1+3\,m/z^2)}{RT\kappa}(\cosh\,[\frac{zq\zeta}{2k_BT}] - 1) \qquad \text{(S–16)}$$

where $\zeta$ is the zeta potential, $D$ the diffusion coefficient of the excess free charge in the diffuse layer, $R$ the gas constant, $k_B$ Boltzmann's constant, $q$ the charge on the electron, $\kappa$ the inverse of the Debye length given by:

$$\kappa = \sqrt{2czF^2/\varepsilon RT} \qquad \text{(S–17)}$$

and $m$ the dimensionless parameter describing the contribution of the ion flux to the diffuse layer surface conductance

$$m = \left(\frac{RT}{F}\right)^2 \frac{2\varepsilon}{3\eta D} \qquad \text{(S–18)}$$

The $K_{diff}$ values can be calculated using eq (S-16) based on the measured $\zeta$ values. Fig. S-1 shows the $\zeta$ values of PS particles and small EVs measured in 0.5 ×, 0.25 ×, and 0.1 × PBS. In 0.5 × PBS, the $\zeta$ values show only minor variations across PS particles of various sizes and small EVs, with the mean values as –16.7 mV for 700 nm particles, –15.0 mV for 500 nm particles, –14.8 mV for 200 nm particles, –12.7 mV for 70 nm particles and –11.6 mV for small EVs (including exosomes, assuming a diameter of 100 nm). The $\zeta$ values show increasing trend with the reduced medium conductivity. The $\zeta$ values also show increasing trend with the increased particle size in 0.1 × PBS. The $\zeta$ values for small EVs fall within the range of –6 mV to –54 mV in concurrence with previously reported values for exosomes isolated from various cell types.[12-14] For PS particles in 0.5 × PBS, respective $K_{diff}$ values vary in the range of 0.2 nS (70 nm) – 0.5 nS (700 nm). These conductance values are slightly lower than those reported for similarly carboxyl-functionalized PS submicron particles in a previous study.[7] This can be attributed to relatively low $\zeta$ values here possibly due to altered surface properties by infused fluorescent dyes. For small EVs in 0.5 × PBS, respective $K_{diff}$ values are approximately 0.2 nS and comparable to the $K_{stern}$ values, yielding a total surface conductance of 0.4 nS. In comparison, previous studies have reported a wide range of surface conductance values for EVs, with values ranging from 6 – 12.5 nS for those derived from more invasive pancreatic tumor cells (BxPC-3 and AsPC-1 cells) to barely discernible levels for those derived from less invasive pancreatic tumor cells (PANC-1 cells) at media conductivities of ~0.03 S/m and above.[6] In the present work, the small EVs and exosomes derived from HEK293T cells exhibited a relatively weak surface conductance similar to the EVs derived from PANC-1 cells.

Fig. S-2 presents the plots of relative polarizability, i.e. Re$\{f_{CM}\}$, of PS particles and small EVs calculated from eqs (S-13) and (S-14) based on the obtained $K_{Stern}$ with $K_{diff}$ values. At the operating frequency of 700 kHz and medium conductivity of 0.75 S/m (0.5 × PBS), particles and small EVs all experience nDEP exhibiting similar polarizability with Re$\{f_{CM}\}$ close to –0.49 for 700 nm particles, –0.44 for 70 nm particles, and about –0.48 for small EVs. Large EVs, with a size ranging from 200 to 1000 nm and a similar composition to small EVs, are also expected to have a negative Re$\{f_{CM}\}$ close to –0.5. At reduced medium conductivities (0.25 × and 0.1 × PBS), surface conductivity plays a dominant role for small particles leading to reduced particle polarization with the magnitude of Re$\{f_{CM}\}$ significantly dropping from –0.44 (in 0.5 × PBS) to –0.2 (in 0.1 × PBS) for 70 nm particles and from –0.48 (in 0.5 × PBS) to –0.3 (in 0.1 × PBS) for small EVs. For 700 nm particles, Re$\{f_{CM}\}$ drops from –0.49 to –0.45. These results indicate that the size-dependent surface conductance effect can lead to changes in the magnitude of nDEP force magnitude for submicron particles and EVs at reduced medium conductivities (0.25 × and 0.1 × PBS).

Lastly, we conducted numerical simulations to obtain the force field of ETF drag and nDEP exerted on 500 nm and 150 nm EVs under an applied activation of $V_{app} = 15$ $\mathrm{V_p}$ at 700 kHz to illustrate the separation mechanism. To account for discrepancies encountered at high voltages and high medium conductivities between experimentally observed ETF velocities and those predicted by the classical model,[15-18] we considered an effective potential of $V_{eff} = \alpha V_{app}$. We specifically chose a value of $\alpha = 0.3$ to match the experimentally measured average ETF velocity of 27.6 μm/s (Movie S-1). This $\alpha$ value is comparable to 0.38 the factor similarly chosen to scale the applied potential to meet experimental ETF velocity in a previous study.[19] For $V_{app} = 15$ $\mathrm{V_p}$, we obtained a magnitude of $\nabla(|\boldsymbol{E}|^2) > 10^{18}$ $\mathrm{V^2/m^3}$, which is within the range of $10^{12}$ to $10^{24}$ $\mathrm{V^2/m^3}$ reported in previous studies.[20-23] Figs. S-3a and S-3b present a side-by-side comparison of the heat maps of the force fields of maximum ETF drag and nDEP exerted on 500 and 150 nm EVs, respectively. A cursory comparison between the corresponding heat maps reveals the likely regions of trapping EVs where nDEP force and ETF drag are comparable near the microelectrodes' upper sidewall segments. While such regions are sizable for 500 nm EVs, they are insignificantly small for 150 nm EVs suggesting that small EVs and exosomes are much less likely to be trapped.

# COMPUTATIONS

The numerical simulations were carried out using COMSOL Multiphysics Software v4.3 (Comsol Inc., Burlington, MA) in a two-dimensional geometry that consisted of a stacked arrangement of layers as shown in Fig. S-4. The layers comprised a 2-mm-thick PDMS cover, an SOI device which featured 75-μm-thick silicon electrodes, 2-μm-thick oxide insulation, and a 500-μm-thick silicon base, a 200-μm-thick double-sided tape, and a 1-mm-thick PCB. The geometry of the channel was discretized with a mesh grid of approximately 1,780,399 domain elements and 12,991 boundary elements as illustrated in Fig. S-4. Further refining the mesh did not significantly affect the solutions, validating the grid-independence of the results.

The Laplace equation was first solved to obtain the quasi-static potential field distribution, which served as the basis for calculating the electric and temperature field distributions using the spatial gradient of the potential field and eq (S-6), respectively. Subsequently, the electrothermal force field per unit volume was computed using eq (S-7), and then treated as the body force in the Stokes equation. The Stokes equation (S-8) was co-solved with the continuity equation (S-9) to derive the flow velocity field and the maximum drag force it exerts on a stationary particle of radius $R$ was calculated using eq (S-10). Eqs (S-11) – (S-18) were utilized to evaluate the DEP force exerted on the particles. Table S-1 lists all the boundary conditions and Tables S-2 and S-3 list the medium and material characteristics used in the simulation, respectively.

MOVIES

**Movie S-1.** Video microscopy and animation of 700 nm fluorescent polystyrene (PS) particles dispersed in 0.5 × PBS in the device channel under nearly stagnant fluid condition during a sinewave voltage activation at 15 $V_p$ and 700 kHz. The animation illustrates the device channel from a cross-sectional view. Particles can be seen circulating under a pair of counter-rotating electrothermal fluid (ETF) rolls. Those in the outer circulations become trapped along the microelectrodes under the influence of negative dielectrophoresis (nDEP), thus leaving a particle-free band along the channel centerline within the first 10 s of the activation. Those polarized in the inner circulations assemble to form pearl chains during the extended activation period. This movie corresponds to Fig. 3A of the main text.

**Movie S-2.** Video microscopy of extracellular vesicles (EVs) undergoing size-based fractionation at the device outlet junction. Small EVs (red; pre-stained with PKH26) and large EVs or microvesicles (green; pre-stained with calcein AM) of an EV mixture are independently shown through corresponding filter sets. In the absence of activation, EVs are seen crossing the outlet junction within a stream focused by the sheath flows, leaving the junction with the main branch. Subsequently, small EVs are seen with their focused stream undergoing defocusing and then refocusing due to ETF rolls as the sinewave voltage activation is gradually increased to 15 $V_p$. Large EVs are seen railing downstream along the microelectrodes under the balance of ETF drag and countering nDEP force, leaving the junction with the side branches. Activation: 700 kHz. Centre and side input flow rates 0.04 and 0.06 mL/h, respectively. Sample and sheath buffers: 0.5 × PBS. This movie corresponds to Fig. 6A of the main text.

FIGURES AND TABLES

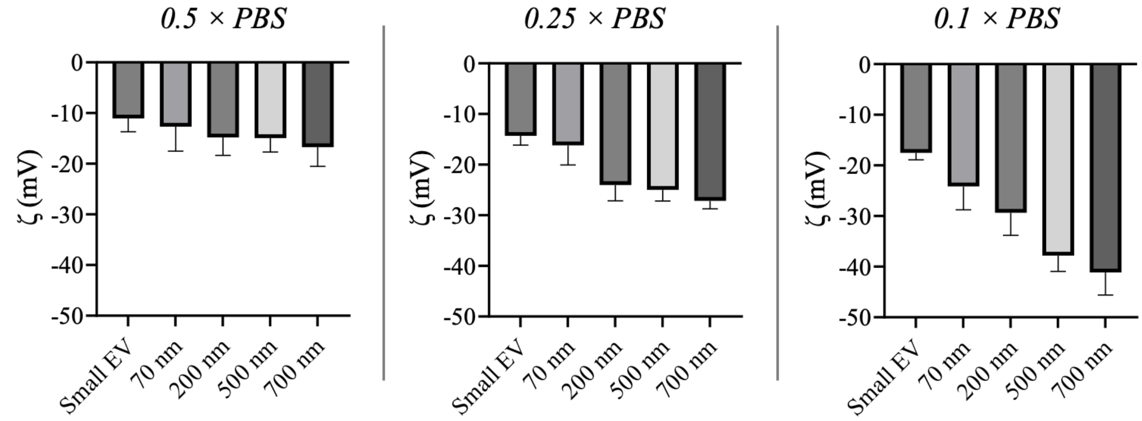

**Figure S-1.** Zeta potential values (mean ± SD, $n = 6$ ) of small EVs (obtained from HEK293T cells) and carboxyl-functionalized fluorescent-tagged PS submicron particles of various size in 0.1×, 0.25×, and 0.5×PBS.

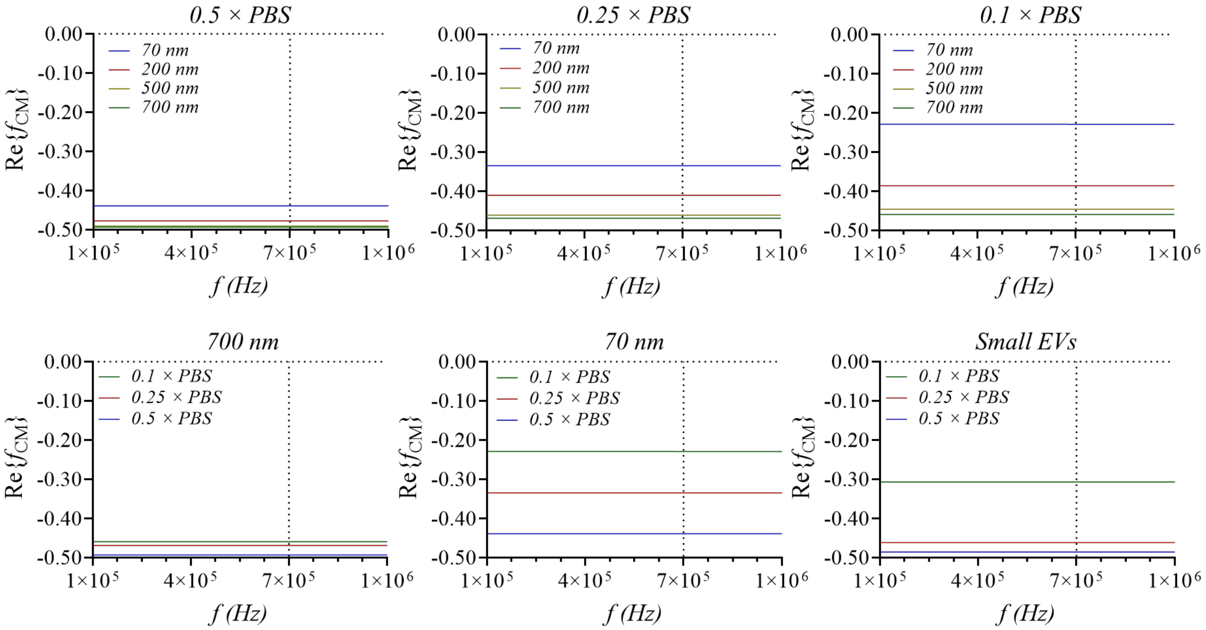

**Figure S-2.** Plots of Re{$f_{CM}$} as a function of the field frequency ranging from 0.1 to 1 MHz for carboxyl-functionalized fluorescent-tagged PS submicron particles of various sizes (legends in upper plots) and small EVs (obtained from HEK293T cells) in the stated PBS buffer (legends in lower plots). Vertical dashed lines mark the operating frequency of 700 kHz.

(a) 500 nm EV

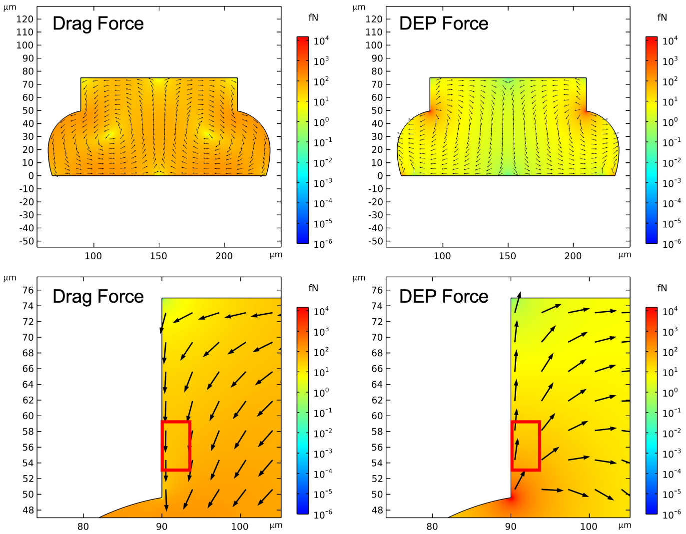

(b) 150 nm EV

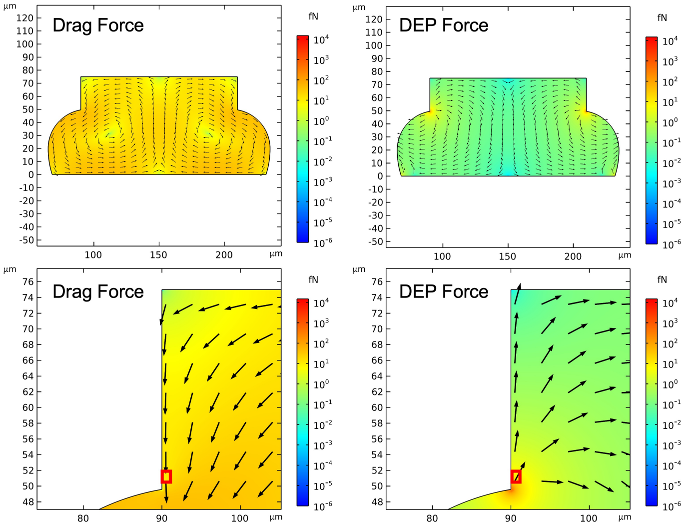

**Figure S-3.** The simulation results showing the maximum ETF drag force (left panels) and nDEP force (right panels) exerted on a (a) 500 nm EV and (b) 150 nm EV in 0.5 × PBS across the fluidic channel for an applied field activation of 15 $V_p$ at 700 kHz (an effective field activation of 4.5 $V_p$ at 700 kHz considered for the computation of ETF drag force to match experimental ETF velocity). Lower panels in (a) and (b) show respective portions of the heat maps (upper panels) in a magnified view with rectangles demarcating the regions where ETF drag and nDEP force are comparable and likely to trap EVs.

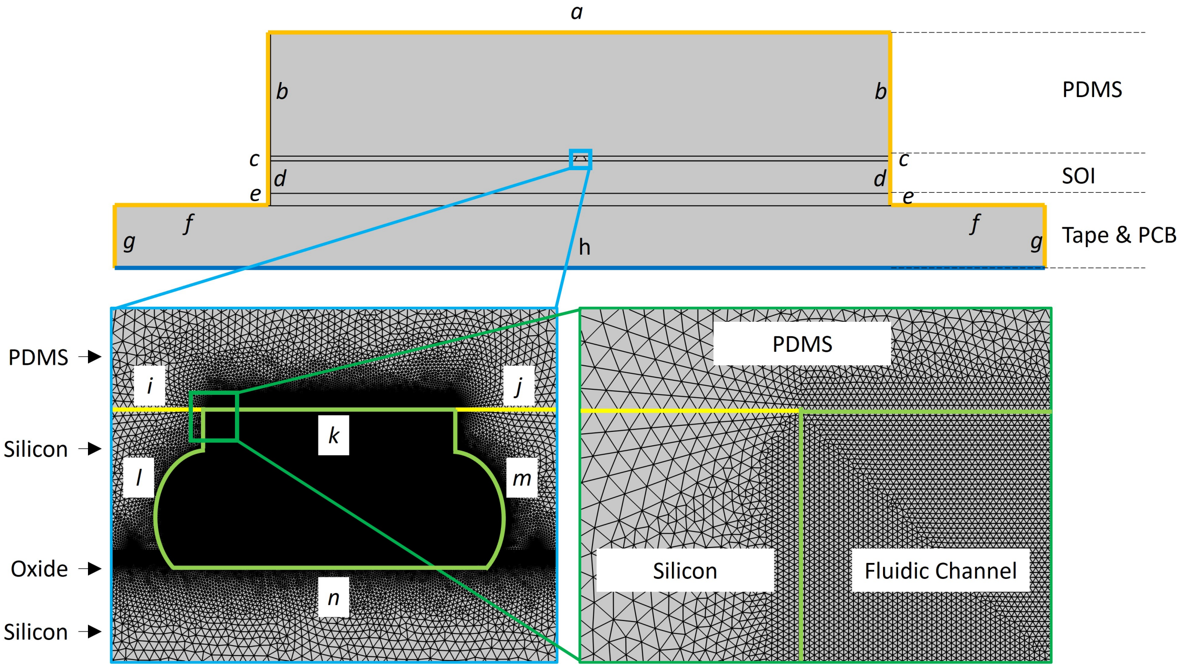

**Figure S-4.** Schematic illustration of the computational domain showing the specified layers and color-coded boundaries that are indexed according to their respective boundary conditions listed in Table S-1. The insets show the distribution of the mesh elements.

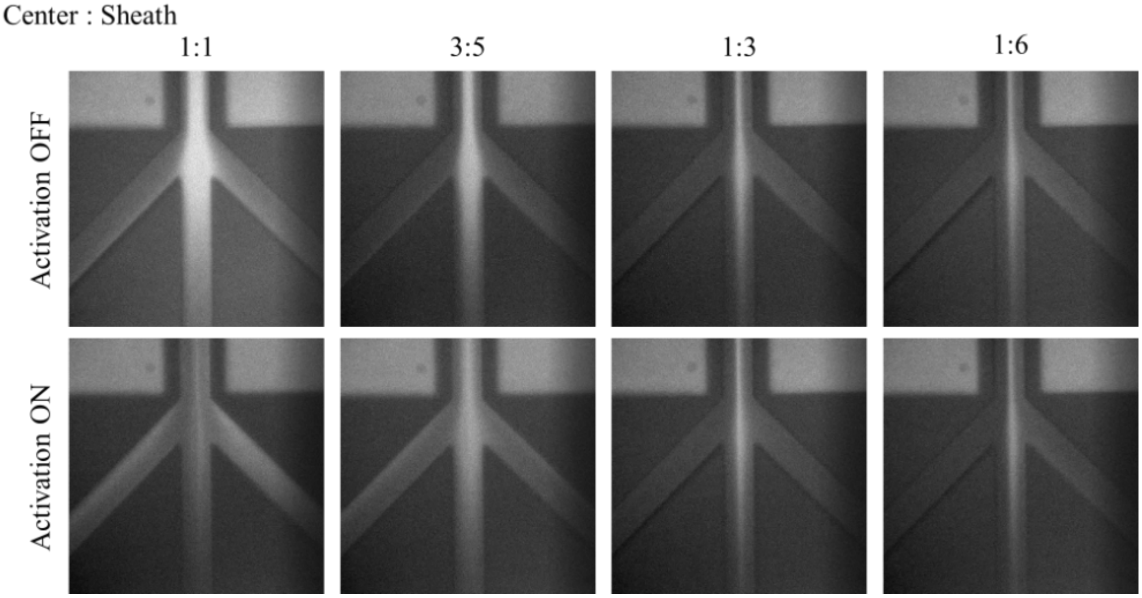

**Figure S-5.** The influence of the ratio of the flow rates of the sample stream to the combined sheath streams (0.5×PBS) on the refocusing behavior 70 nm polystyrene particles at the outlet junction under a sinewave activation (700 kHz at 15 $V_p$) and with a constant total flow rate (0.16 mL/h). For example, sample: sheath = 1:1 refers to the ratio where the sample flow rate is 0.08 mL/h and the sheath flow rate is 0.08 mL/h with either sheath stream delivered at 0.04 mL/h. Fluorescent images of the outlet junction for respective ratios of flow rates are shown with the activation OFF (upper row) and ON (lower row). Sample and sheath buffers: 0.5 × PBS.

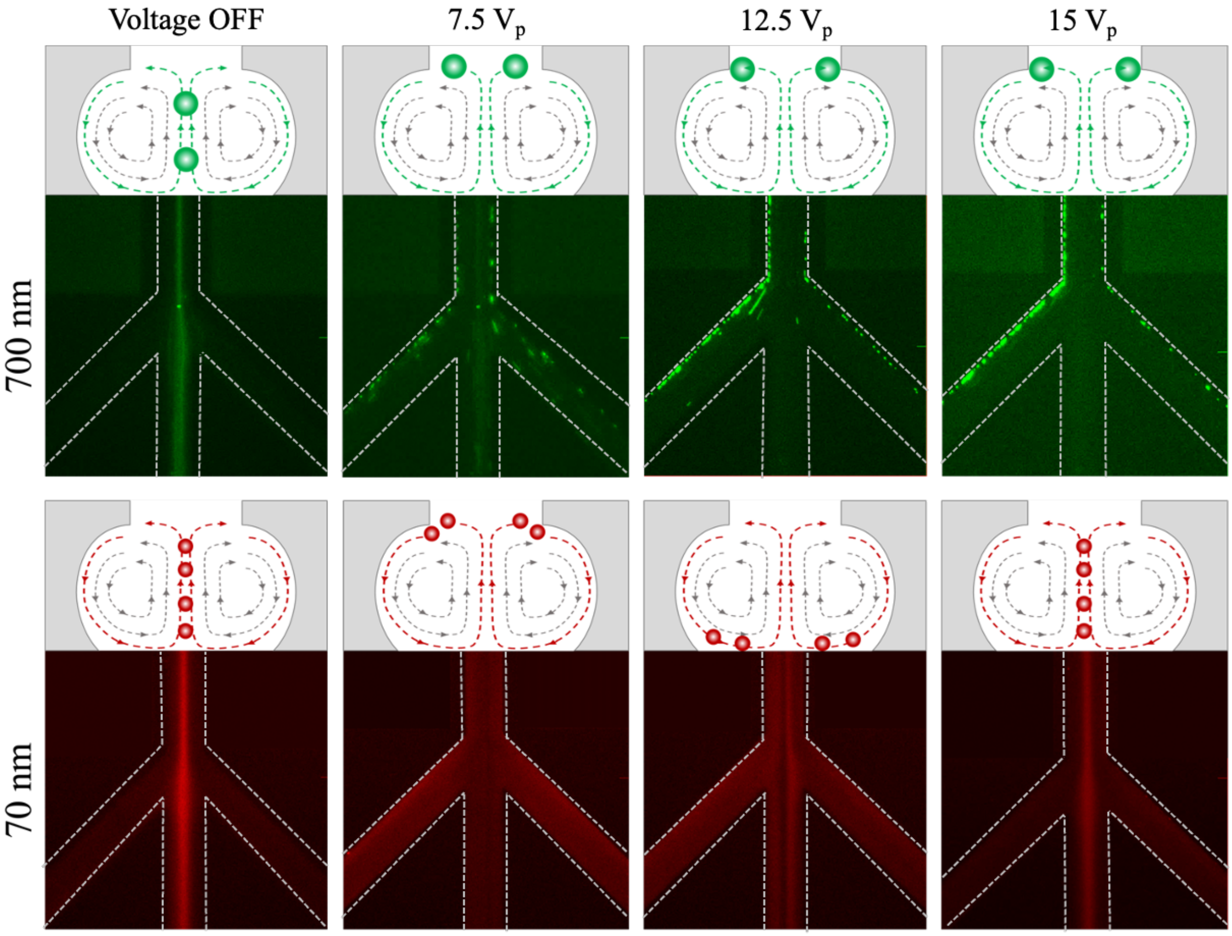

**Figure S-6.** Fluorescent images and corresponding channel cross-sectional schematics describing the stream of 700 nm PS particles (upper row) in comparison to the stream of 70 nm PS particles (lower row) at the outlet junction in the absence and presence of sinewave voltage activation at 700 kHz and with a peak voltage as stated. Centre and side input flow rates 0.04 and 0.06 mL/h, respectively. Sample and sheath buffers: 0.5 × PBS.

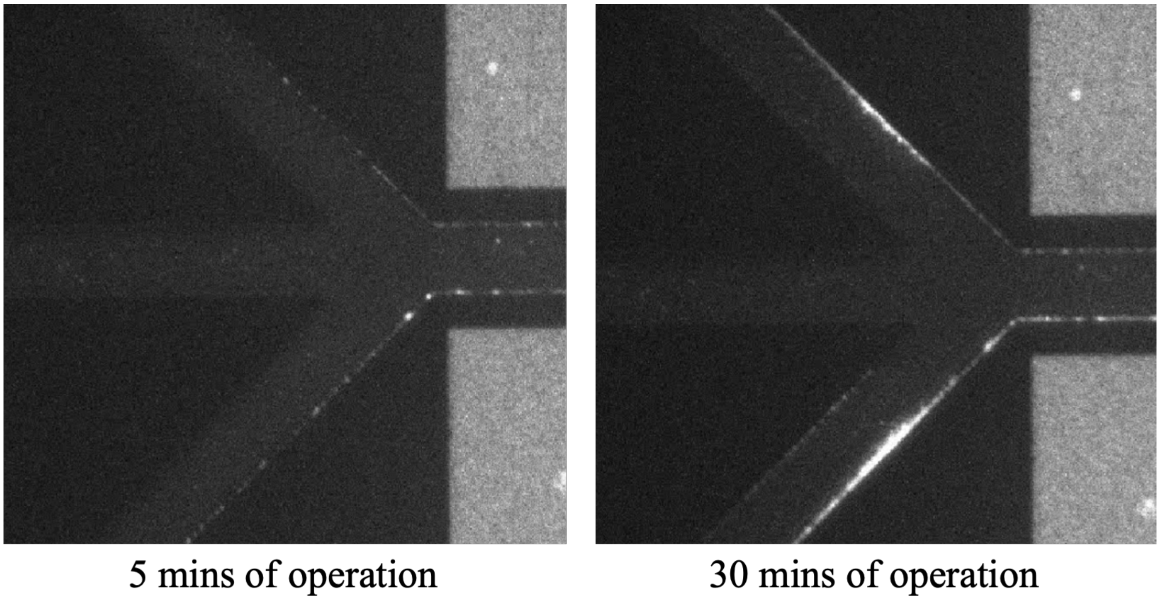

**Figure S-7.** Fluorescent images showing large EVs (green; pre-stained with Calcein AM) at the outlet junction captured at 5 and 30 mins after the onset of the separation process. Large EVs can be seen accumulated and immobilized on the electrode sidewalls in the side branches. Activation: 700 kHz at 15 $V_p$. Centre and side input flow rates 0.04 and 0.06 mL/h, respectively. Sample and sheath buffers: 0.5 × PBS.

**Table S-1** Boundary conditions used for the 2D computational domain, Figure S-4.

| Boundary | Electrical | Thermal | Fluidic |
|---|---|---|---|
| $\boldsymbol{a}$ - $\boldsymbol{g}$ | Electric insulation | Convective cooling | - |
| $\boldsymbol{h}$ | Electric insulation | Room Temperature | - |
| $\boldsymbol{i, j}$ | Electric potential | Continuity | - |
| $\boldsymbol{k, l, m, n}$ | Continuity | Continuity | No slip |

**Table S-2** Medium characteristics used in the simulations.

| Characteristics | 0.5× PBS* |
|---|---|
| Dynamic viscosity (Pa·s) | $1.38 - 0.02T + 1.36 \times 10^{-4}T^2 + 4.65 \times 10^{-7}T^3 + 8.90 \times 10^{-10}T^4 - 9.08 \times 10^{-13}T^5 + 3.85 \times 10^{-16}T^6$ |
| Electrical conductivity (S m$^{-1}$) | 0.75 |
| Specific heat capacity (J·kg$^{-1}$K$^{-1}$) | $12010.15 - 80.41T + 0.31T^2 - 5.38 \times 10^{-4}T^3 + 3.63 \times 10^{-7}T^4$ |
| Density (kg·m$^{-1}$) | $-950.70 + 18.92T - 0.06T^2 + 6.31 \times 10^{-5}T^3$ |
| Thermal conductivity (W·m$^{-1}$K$^{-1}$) | $-0.87 + 8.95 \times 10^{-3}T - 1.58 \times 10^{-5}T^2 + 7.98 \times 10^{-9}T^3$ |
| Relative permittivity | 80 |

* The unit of temperature ($T$) is Kelvin.

**Table S-3** Material characteristics used in the simulations.

| **Characteristics** | **Si** | **$SiO_2$** | **PDMS** | **PCB (FR-4)** |
|---|---|---|---|---|
| Specific Heat Capacity ($J\cdot kg^{-1}K^{-1}$) | 700 | 1000 | 1460 | 1369 |
| Relative permittivity | 11.7 | 3.8 | 1 | 1 |
| Density ($kg\cdot m^{-3}$) | 2329 | 2650 | 970 | 1900 |
| Thermal conductivity ($W\cdot m^{-1}K^{-1}$) | 149 | 1.3 | 0.16 | 0.3 |
| Electrical conductivity ($S\cdot m^{-1}$) | 2E4 | 1E-16 | 2.5E-14 | 4E-3 |

# REFERENCES

1 A. Castellanos, A. Ramos, A. González, N. G. Green and H. Morgan, *J. Phys. D,* 2003, **36**, 2584-2597.

2 Y. Lu, Q. Ren, T. Liu, S. L. Leung, V. Gau, J. C. Liao, C. L. Chan and P. K. Wong, *Int. J. Heat Mass Transf.,* 2016, **98**, 341-349.

3 T. B. Jones, *Electromechanics of particles*, Cambridge Univ. Press, 1995.

4 H. Morgan and N. G. Green, *AC electrokinetics: colloids and nanoparticles*, Research Studies Press, 2003.

5 H. A. Pohl, Dielectrophoresis: *The behavior of neutral matter in nonuniform electric fields*, Cambridge Univ. Press, 1978.

6 J. H. Moore, W. B. Varhue, Y. Su, S. S. Linton, V. Farmehini, T. E. Fox, G. L. Matters, M. Kester and N. S. Swami, *Anal. Chem.,* 2019, **91**, 10424-10431.

7 I. Ermolina and H. Morgan, *J. Colloid Interface Sci.,* 2005, **285**, 419-42.

8 M. P. Hughes and N. G. Green, *J. Colloid Interface Sci.,* 2002, **250**, 266-268 .

9 Q. Chen and Y. J. Yuan, *RSC Adv.,* 2019, **9**, 4963-4981.

10 H. Woo, Y. K. Cho, C. Y. Lee, H. Lee, C. M. Castro and H. Lee, *Theranostics,* 2022, **12**, 1988-1998.

11 I. I. Hosseini, Z. Liu, X. Capaldi, T. AbdelFatah, L. Montermini, J. Rak, W. Reisner and S. Mahshid, *Nano Lett.,* 2021, **21**, 4895-4902.

12 M. Kesimer and R. Gupta, *Methods,* 2015, **87**, 59-63.

13 G. Midekessa, K. Godakumara, J. Ord, J. Viil, F. Lättekivi, K. Dissanayake, S. Kopanchuk, A. Rinken, A. Andronowska, S. Bhattacharjee, T. Rinken and A. Fazeli, *ACS omega,* 2020, **5**, 16701-16710.

14 T. Soares Martins, J. Catita, I. Martins Rosa, A. B. Silva, Odete and A. G. Henriques, *PLoS ONE,* 2018, **13**, e0198820.

15 Y. Lu, Q. Ren, T. Liu, S. L. Leung, V. Gau, J. C. Liao, C. L. Chan and P. K. Wong, *Int. J. Heat Mass Transf.,* 2016, **98**, 341-349.

16 M. L. Y. Sin, V. Gau, J. C. Liao and P. K. Wong, *J. Assoc. Lab. Autom.,* 2010, **15**, 426-432.

17 F. J. Hong, J. Cao and P. Cheng, *Int. Commun. Heat Mass Transf.,* 2011, **38**, 275-279.

18 S. Loire, P. Kauffmann, I. Mezi and C. D. Meinhart, *J. Phys. D: Appl. Phys.,* 2012, **45**, 185301-7.

19 H. C. Feldman, M. Sigurdson and C. D. Meinhart, *Lab Chip,* 2007, **7**, 1553-1559.

20 R. Hölzel and R. Pethig, *Micromachines,* 2020, **11**, 533.

21 R. Hölzel, N. Calander, Z. Chiragwandi, M. Willander and F. F. Bier, *Physical review letters,* 2005, **95**, 128102.1-128102.4.

22 X. Xing, R. Y. Poon, C. S. Wong and L. Yobas, *Biosens. Bioelectron.*, 2014, **61**, 434-442.

23 X. Xing and L. Yobas, *Analyst*, 2015, **140**, 3397-3405.